ORIGINAL ARTICLE

CrossMark

Influences of *z*-axis increment and analyses of defects of AISI 316L stainless steel hollow thin-walled cylinder

Tianbiao Yu[1] · Jiayu Sun[1,2] · Wanrui Qu[3] · Yu Zhao[1] · Lin Yang[1]

Abstract

In the present paper, AISI 316L stainless steel hollow thin-walled cylinders were fabricated via laser engineered net shaping (LENS), which have been described in details. It is found that *z*-axis increment (delta Z) has significant effects on the geometrical features, mechanical, and metallurgical properties via single factor experiment in the condition of optimized processing parameters (laser power, powder feed rate, shielding gas flow rate and scanning speed) unchanged. Therefore, it is observed that deviations of the diameter are caused by unstable working distance, inclination angles, and preheating condition. As a result, through analyzing and modifying structural defects, an optimized delta Z, practical scanning strategies, and high surface quality of the cladding hollow thin-walled cylinder have been obtained. Expanding these conclusions to more complex build geometries and a more comprehensive variety of processing conditions would allow for a better understanding of the laser deposition process for more ubiquity of LENS in the industry.

1 Introduction

Additive manufacturing (AM) technology is one kind of processing method, joining materials to make parts layer upon layer from 3D models directly [1]. Among all the methodologies of AM, laser engineered net shaping (LENS) has become the most practical method owing to its competitive edge of easy controllability, predominant surface quality, high practicality, excellent forming efficiency, high powder utilizing efficiency and outstanding stability, etc. [2]. AISI 316L is also one kind of widely investigated materials applied to marine and biomedical equipment [2–4].

Many researches have evaluated the significance of *z*-axis increment (ΔZ) via fabricating thin walls. Li et al. [5]

investigated and optimized this parameter and accomplished fine surface quality, mechanical properties, and metallurgical behaviors. Meanwhile, Hollow thin-walled cylinder is a no negligible model to evaluate ΔZ and used in his paper. Petrat et al. [6] indicated hollow cylinder with three different sizes of height, wall thickness, and diameter to find the relationship among them. It was claimed that changes of starting point between inner and outer edge and ΔZ were needed for a constant component growth. Qi et al. [7] found that the maximum stable layer height would ensure a stable deposition process for each investigated condition via a full-factorial central composite design (CCD) experiment and obtained the linear regression for the maximum stable height increment. Abioye et al. [8] built a functionally graded cylinder to analyze metallurgical properties of different materials and demonstrated that it was possible to fabricate functionally graded structures using various ΔZ. Also, excessive heating would cause the flattening feature of layers, making the preset ΔZ incorrect and deteriorating the process stability. Niu et al. [9] discovered the structural defects, which made the shape like a "dumbbell," then fabricated the hollow cylinders via optimal processing parameters including *z*-axis increment. Durejko et al. [10] obtained a high metallurgical quality and a good reproduction of cladding hollow tubes applying modification of the code. Also, it was found that numerous cracks were a common

✉ Tianbiao Yu
tianbiaoyudyx@gmail.com

[1] School of Mechanical Engineering and Automation, Northeastern University, NO. 3-11, Wen hua Road, He ping District, Shenyang 110819, People's Republic of China

[2] Deformation Processing Institute for Materials Research, Tohoku University, Sendai, Japan

[3] Department of Mechanical Engineering, University of Alberta, Edmonton T6G 2R3, Canada

defect observed in received samples, especially near the substrate zone due to multiply Z-heights. From Lima et al. [11], it could be seen that when superposed, more and more sequential layers, structure defects, and metallurgical problems occurred due to the heat gathering in processing thin cladding layers of stainless steel. Calleja. et al. [12] analyzed the ΔZ standoff, using the optical profilometer in five different sections of the cladding to measure this parameter. Different standoff values were tested (0.2–0.4–0.6–0.8), and the best results were obtained for 0.4 mm. Bi et al. [13] discovered that both the deposition process and the measured temperature signal depended strongly on the Z-increment. The variation of the melt pool temperature and the Z-increment resulted in an inhomogeneous dimensional accuracy, microstructure, and hardness of the deposited sample.

These relevant literatures all put meaningful efforts on one or more research aspects of the thin-walled stainless steel parts, either the effects of ΔZ or the performances of metallurgical defects, either the control of geometrical precision or the improvement of surface finish. However, this paper puts efforts to operate systematic experiments and comprehensive analyses of ΔZ on the thin-walled structures to grasp the characteristics of microstructure, and master the influence rules of deviations on microstructure morphology, and then optimize the technological process to compensate previous studies.

2 Experimental details

In order to analyze the geometrical features of hollow thin-walled cylinder, mechanical and metallurgical properties according to various ΔZ, meanwhile, evaluate and modify geometrical defects to obtain finer shape and surface quality, single factor experiment according to ΔZ was conducted with laser power, powder feed rate, shielding gas flow rate, and scanning speed unchanged in Table 1 to analyze the effects of changing ΔZ. To optimize the processing parameter ΔZ, the deviations between the measured value of the inside/outside diameter and the mean value and the deviations between actual inside/outside diameter, width, and the theoretical value were planned to be obtained. Via comparing these deviations, the optimal processing parameter combining with ΔZ could be testified for future study. Hence, apart from ΔZ, other elements such as working distance, inclination angles, and preheating condition would validate their effects on the processing quality.

2.1 Experimental setup and materials

During the LENS process, argon gas is used as shielding gas and powder delivery gas. Metal powder is delivered by argon gas and melt in the molten pool radiated by laser beam, meanwhile, the nozzle can deliver shielding gas to protect the

Table 1 Processing parameters and measured values

Name	Unit	Value
Laser power (P)	W	350.000
Scanning speed (V_s)	mm/s	5.500
Powder feed rate (V_f)	g/min	11.650
Shielding gas flow rate (G)	L/h	15.000
Height of the one layer (H)	mm	0.316
Width of one layer (b)	mm	1.130
Radius of the powder jet	mm	0.093–0.150
Radius of the laser beam (d)	mm	1.000
Density of powder	kg/m^3	4520.000
Scanning diameter	mm	20.000

molten pool from oxidation. After deposition of the first layer, the second layer consecutively fabricates on the former layers, which can be regarded as a new substrate for latter layers (Fig. 1b).

The material of substrate is steel C1045 with a dimension of 100 mm × 100 mm × 12 mm, and the material of cladding powder is AISI 316L stainless steel. The experimental equipment (Fig. 1a) consist of one continuous wave fiber laser generator (less than 500 W, power instability rate is ±5%, calibration wavelength is 1064 nm, detector photosensitive surface diameter is 200 mm, minimum resolution is 1 W, the response time and recovery time are both ≤3.0 min, maximum peak power density is 6 MW/cm^2) with laser direct fabrication (LDF) system, one KUKA robot (KUKA ZH30/60III) with deposition head and nozzle (Collimation focal length is 100–125 mm, focus focal length is 250–300 mm, working distance is less than 15.5 mm), one water cooler, one powder feeder (range of sending powder particle size is 0.074–0.159 mm, range of powder disk speed is 0–5.8 r/min), and one workbench. The hardware and computer software of devices provide stable and effective assistance.

2.2 Theories and primary selection of delta Z

Significantly, ΔZ is a predominant parameter to determinate and ensure cladding quality, mechanical properties, and metallurgical behaviors. Appropriate ΔZ can improve the melting defects of the previous layers, forming a good metallurgical combination between layers, or else would cause undesirable fusion defects. An optimal processing strategy has been obtained from previous research, and the value of four process parameters and measured values are shown in Table 1.

The figure of the cross section of one single cladding layer is shown in Fig. 2a. As described in Fig. 2b, H signifies the height of single cladding layer and b denotes the width of single cladding pass, which was measured using metallographic cross sections of the parts after polishing and chemical corrosion by Olympus laser confocal instrument (Light source

Fig. 1 Illustration of experimental setup and schematic of LENS. **a** Experimental setup. **b** Schematic of the manufacturing process
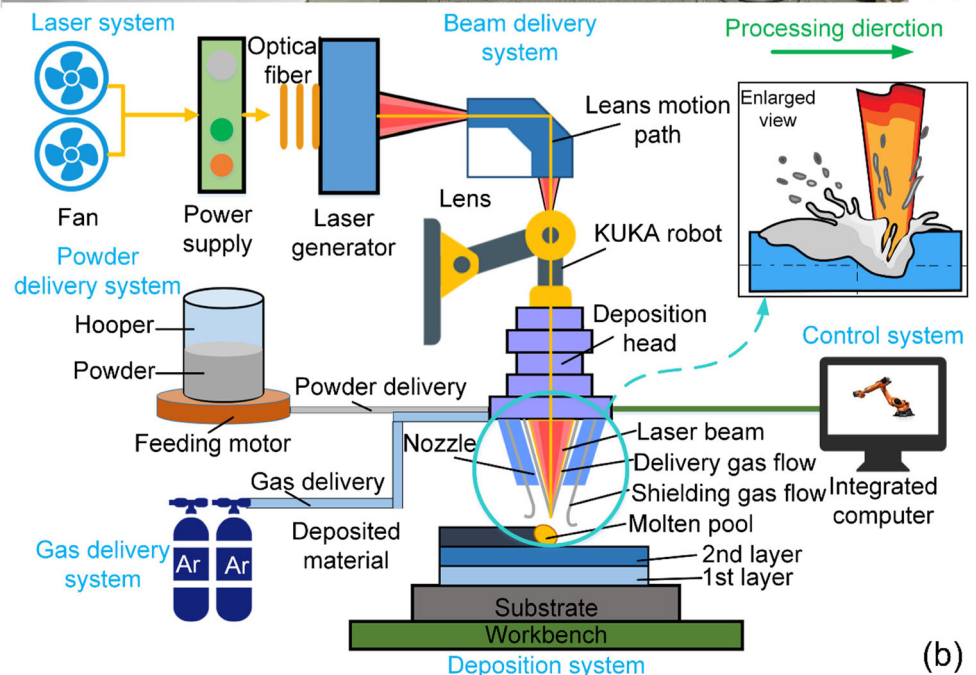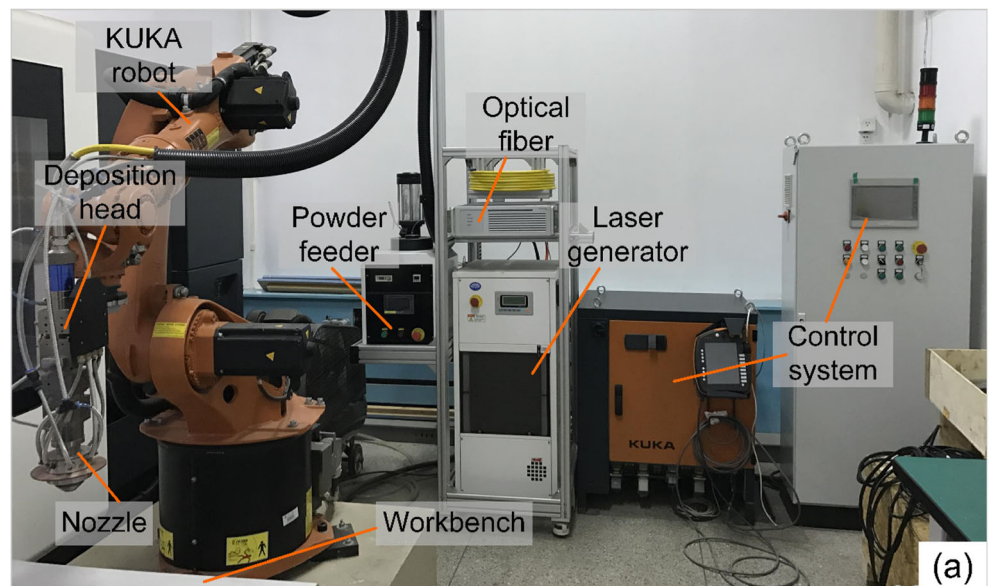
is 405 nm semiconductor laser zoom, optical zoom is from 1× to 8×, total magnification is ×108–×17,280).

The first cladding layer can be regarded as a part of a circle [14], in order to obtain an ideal multilayer model, with the remelting area CDE of one of two consecutive layers equals to the surrounding rectangular area ABCD (Fig. 2c). Eqs. (1) and (2) are as follows.

$$S_1 = S_{CDE} = S_{ABCD} = \Delta Z \times b \qquad (1)$$

$$\Delta Z = \frac{1}{64H^2 b}\left[\left(4\mathrm{H}^2 + b^2\right)^2 \times \arcsin\left(\frac{4bH}{4H^2 + b^2}\right) - 4Hb\left(b^2 - 4H^2\right)\right] \qquad (2)$$

Where S_1 is the cross-sectional area of the first cladding layer, H_1 is the height of the first layer; S_2 is the cross-sectional

area of the second cladding layer, H_2 is the height of the second layer. Theoretical ΔZ_1 can be obtained via Eq. (2). Therefore, $\Delta Z_1 \approx 0.224$mm. The measured height of the cladding layer can be regard as an actual value. So, $\Delta Z_4 = H = 0.316$ mm [5]. Then, select two intermediate values as experimental parameters. It is verified that H_2 is less than H_1, ΔZcan also be regarded as H_2 due to impacts of surface tension and gravity. That is, ΔZ is less thanH_1. Therefore, $\Delta Z_2 = 0.316 - 0.05 = 0.266$mm is designed to present intermediate value according to Peng Li [15] and $\Delta Z_3 = 0.307$ mmwas selected randomly. Laser energy density (E) in joules per kilogram is as follows.
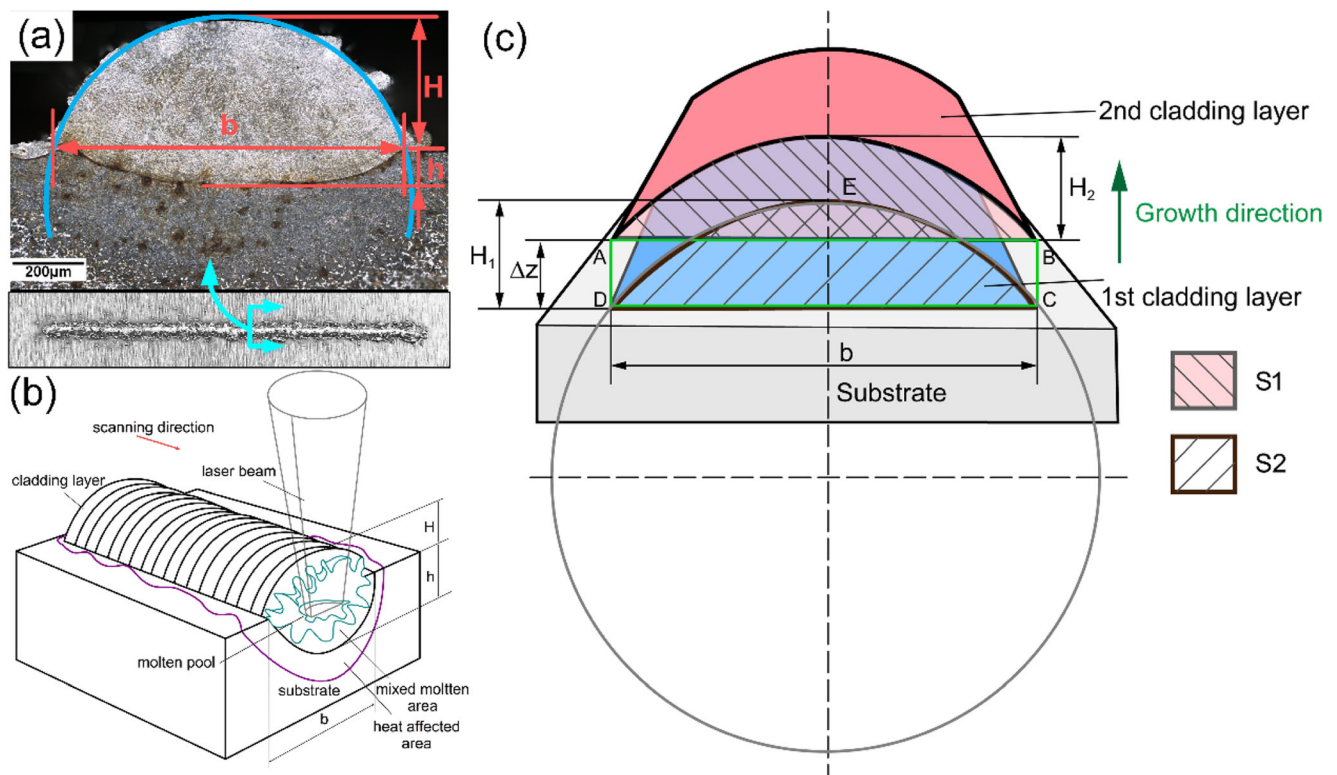
$$E = P/V_s \times d \qquad (3)$$

Fig. 2 Introduction of measurement parameter. **a** Cross section. **b** Schematic diagram. **c** Multilayer model of two consecutive layers

Where variables are shown in Table 1. As we all know, ΔZ is closely related to H. If $\Delta Z > H$, the defocusing amount is larger, the effective spot diameter is larger, causing E to gradually increase, and the weld width would be larger. The forming process gradually deviates from the equilibrium, resulting in lower precision parts and leading to failure of cladding process. If $\Delta Z < H$, the width of the cladding layer and the melting height of the cladding layer become smaller. With the increase of the cladding layers, the process would continue to balance H with ΔZ. Also, the compensation from balanced layers would be able to obtain better morphology. However, if $\Delta Z \ll H$, the forming parts cannot meet the predetermined height and would lead to poor fusion phenomenon and defective structures.

2.3 Selection of the scanning path

Undeniably, the laser scanning path is also a predominant factor to affect forming quality. As shown in Fig. 3 for defective thin-walled parts, there are serious geometrical defects such as flanging, warping, and bending features; deformation and collapsed edge; and irregularly uneven surface. There exist various reasons. First, the starting points of the suboptimal scanning paths are always in a place without changing. The nozzle accelerates and decelerates due to the presence of acceleration at the beginning and at the end of the program, causing gradually changeable laser scanning speed at both ends, while extending the processing time at both ends. As a

result, this phenomenon causes the starting points of the cladding row to increasingly lift. Second, unseasonable ΔZ would result in repeated remelting, flanging, and bending of top edges. It is difficult to get a fine surface quality.

In order to alleviate such defects and obtain fine geometrical features, using the "Distance Farthest" (DF) mechanism of the starting point, which ensures starting points between two continuous layers are farthest (Fig. 4a).

The clockwise scanning direction and starting as well as ending point 1 of the first layer are shown in Fig. 5a. According to the DF mechanism, the starting and ending point of the second layer is point 2, which is located at the far most region from point 1. Also, there are four sections to define cooling time in accordance with the processing direction, region IV means cooling for four periods of time, region III means cooling for three periods of time, which is lesser than IV, and so on. As a result, if the second layer would take a clockwise processing direction, then it will start from region II (Fig. 5b). On the contrary, if the second layer would take an anticlockwise processing direction, then it would start from region III (Fig. 5c). So, we regard the equidirectional process as "Hot Overlapping" (HO) and reversal process as "Cold Overlapping" (CO) according to their length and statement of cooling time.

3 Results and discussion

To analyze the effect of ΔZ on cladding quality and optimize this processing parameter while other four parameters in
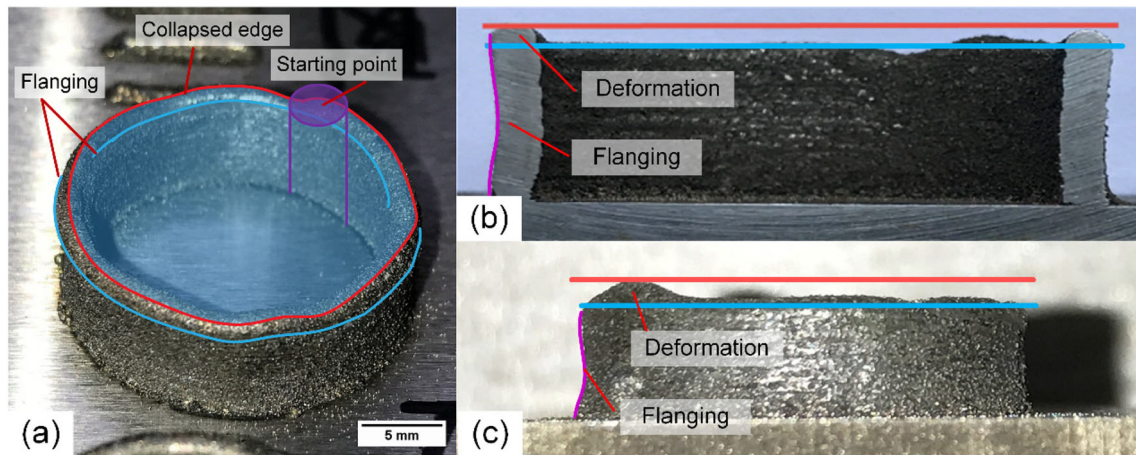
Fig. 3 Defective thin-walled parts. **a** Isometric side view. **b** Sectional view. **c** Front view

Table 1 remain constant, we did a single factor test and cladding each layer with a diameter of 20-mm single ring for 20 layers, this experiment was conducted five times to obtain a statistically meaningful conclusion. That is, each cylinder was fabricated five times repeatedly. Also, two kinds of scanning methods (HO and CO) and DF mechanism of the starting point were applied, respectively. The topography of seven cylinders of each experiment is shown in Fig. 6 with five diverse views.

In Fig. 6, the highest point and the lowest point are presented by pink wireframes, indicating the top surface defects. Also, these wireframes indicate the apparent height difference of the top, the larger the height, the more serious top subsidence is. As a result, larger wireframes are observed in specimen 5 and specimen 7, that is, these two specimens have even worse geometrical structures and forming quality.

The vertical red wireframes mean the width of thin-walled range, the outer side of the wireframe is the widest point, and inside of the wireframe is the narrowest point. The width of the frame represents the degree of defect in width; larger width means that cladding effect is worse. Specimen 4 and specimen 7 are observed larger wireframe and wave top surface, which

means these two specimens have a great chance to encounter flanging and bending phenomenon, top subsidence, and collapsed edge. In the sectional view, as the same, the red line marked the top of the highest point, the blue line marked the top of the lowest point, which also represents the deviation on the top.

3.1 Effects of delta Z on width

Every five layers of the inner wall width and the outer wall width were measured by a three-point diameter measuring instrument, a total of four groups, both inside and outside the thin walls, were measured three times at eight division points to get the inner and outer diameter mean value. Additionally, the height mean value was measured from the eight points from the top surface to the bottom of the substrate. (Fig. 7).

The correctness of the data was verified by analyzing the measured data of the diameters and the deviations. Each of the specimen was measured at the bottom layers (five layers), middle and lower layers (five layers), middle and upper layers (five layers), and upper layers (five layers), a total of four
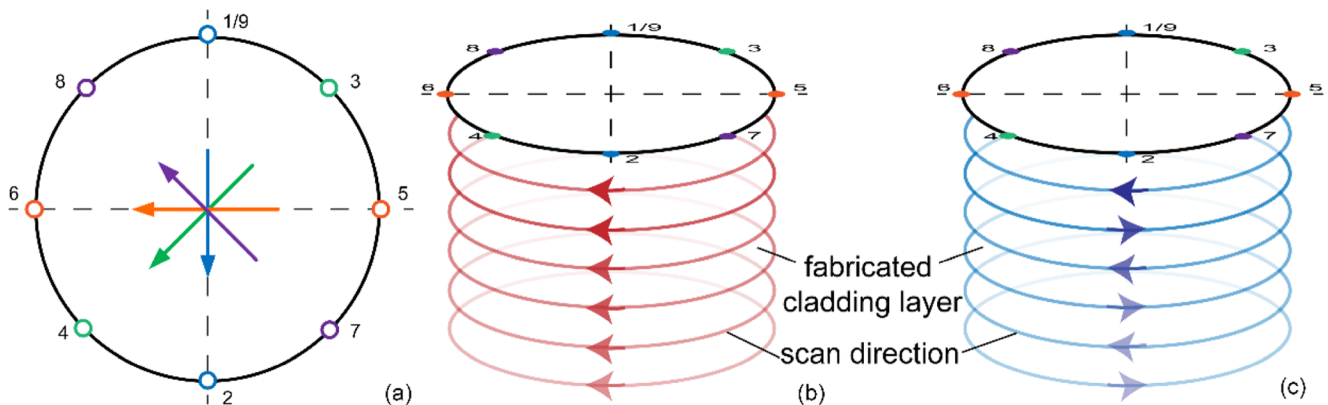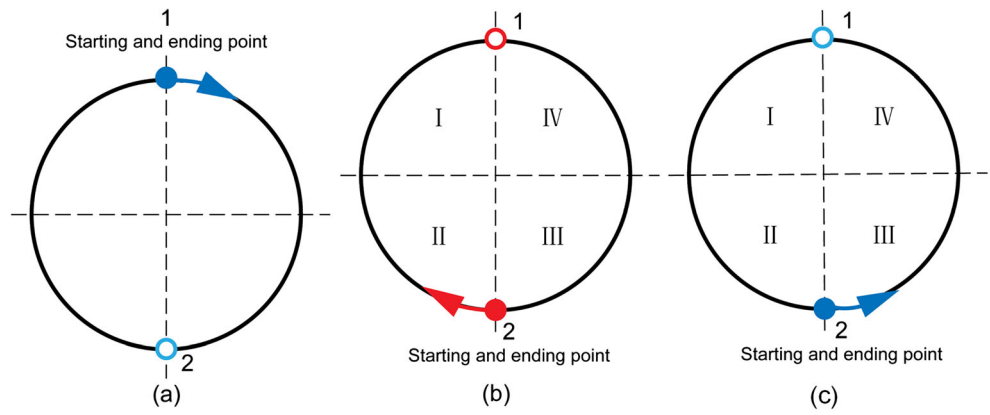

Fig. 4 Design of scanning method. **a** Schematic figure of DF mechanism of starting point. **b** Equidirectional hot overlapping. **c** Reversed cold overlapping

Fig. 5 Cooling time analysis of equidirectional and reversed overlapping. **a** 1st layer. **b** 2nd layer - equidirectional. **c** 2nd layer - reversal

groups. Then, the mean values of each group were calculated by five repeated experiments. As a result, a total of 12 sets of data respectively were obtained (Table 2).

It can be found that the wall thickness is larger than the theoretical spot diameter, because the powder absorbs the energy from the laser irradiation region and increases the amount
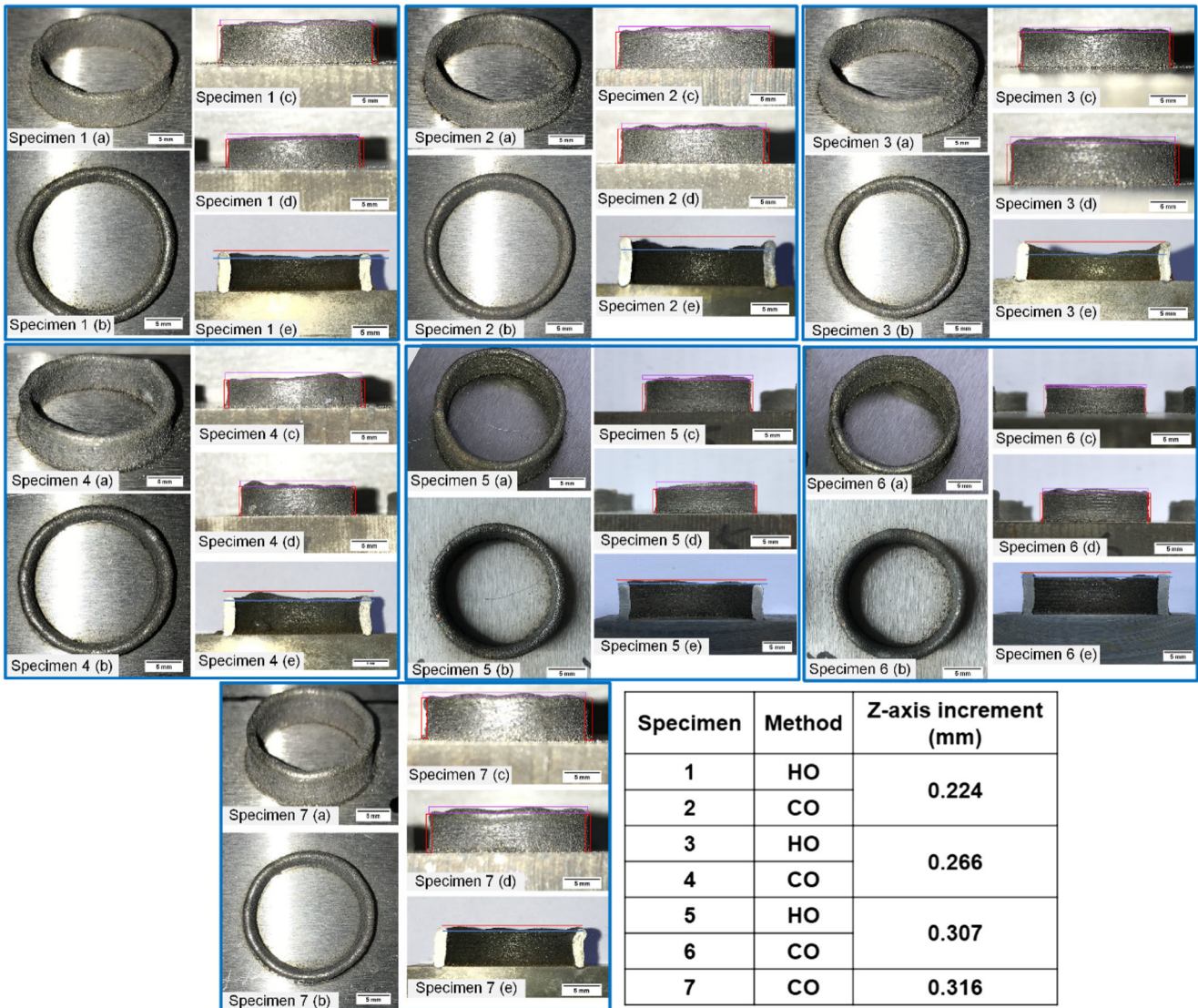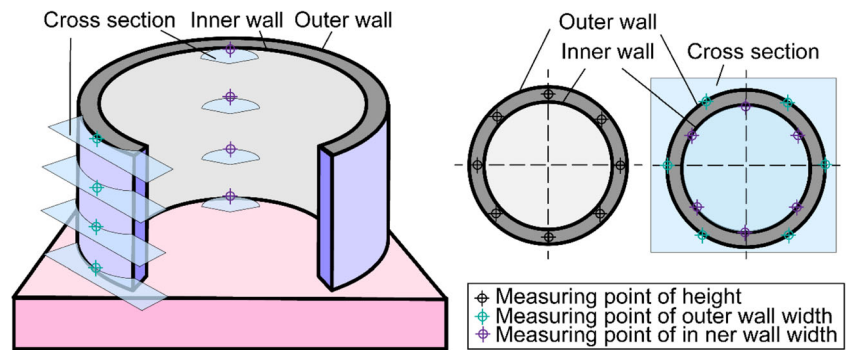

Specimen	Method	Z-axis increment (mm)
1	HO	0.224
2	CO	
3	HO	0.266
4	CO	
5	HO	0.307
6	CO	
7	CO	0.316

Fig. 6 Topography of seven hollow thin-walled cylinders. **a** Isometric side view. **b** Top view. **c** Front view. **d** Left view. **e** Sectional view

Fig. 7 Schematic figure of measurement arrangement

of the metal powder by the heat transfer. So that the surrounding areas of the laser spot are heated and the cladding widths increase, which makes the pool area expand and wall thicknesses increase.

From Fig. 8, straight thin-walled parts were fabricated and used the processing parameters in Table 1 to define mean width value as theoretical width. As a result, theoretical width was reset as 1.8 mm from the previous measurement. So, theoretical outside diameter is 21.8 mm as well as theoretical inside diameter is 18.2 mm. Therefore, specimens 5, 6, and 7 have a large deviation on the wall thickness.

The results and deviations of each specimen in Table 2 can be interpreted vividly via the deviation bands of inside diameters, outside diameters, and the order of mean values from Figs. 9 to 12 in each small figure of each specimen. The red lines in each small figure mean the mean value of 20 layers, and the black lines signify the mean value of five bottom layers and five top layers, respectively. In Figs. 9 to 12, the standard mean indicates the same meaning of theoretical values. According to the order of mean values, the distance between the standard mean and the mean value of each specimen determines the accuracy.

### 3.1.1 Comparison of measured inside diameters with mean values

The conclusions are as follows.

1. HO has better forming quality. In Fig. 9, a smaller deviation band can be observed from specimen 1 to specimen 5, which are fabricated via both HO and CO cladding condition. At the same time, the fluctuations of the curves of these five specimens are less than specimens 6 and 7, which indicates that these five specimens have better stability and cladding quality. However, the mean values of HO (specimen 5, specimen 3, and specimen 1) are higher than the CO cladding, which means that the deviation of CO cladding specimens from the standard value (theoretical mean value) is bigger than the HO cladding condition. It is well known that HO can effectively avoid the poor appearance of fabricated parts because of the continuous remelting, making the powder attach to the surface in the molten pool to improve the quality.

2. The upper deviation of the inside diameter is larger, while the middle and bottom deviations are smaller. Because the

Table 2 Measurement of different z-axis increments

Item (mm)	1	2	3	4	5	6	7
Method	HO	CO	HO	CO	HO	CO	CO
ΔZ	0.224		0.266		0.307		0.316
Mean inside diameter	17.612	17.533	17.677	17.543	17.705	17.492	17.380
Deviation	0.115	0.154	0.145	0.202	0.120	0.080	0.220
Theoretical inside diameter	18.200						
Deviation	− 0.588	− 0.667	− 0.523	− 0.657	− 0.495	− 0.708	− 0.820
Mean outside diameter	21.226	21.221	21.165	21.078	21.267	21.183	21.183
Deviation	0.187	0.116	0.115	0.147	0.123	0.109	0.183
Theoretical outside diameter	21.800						
Deviation	0.574	0.579	0.635	0.722	0.533	0.617	0.617
Center diameter	19.436	19.377	19.421	19.311	19.486	19.333	19.282
Deviation	0.564	0.623	0.579	0.689	0.514	0.667	0.718
Wall thickness	1.807	1.824	1.768	1.744	1.881	1.876	1.901
Deviation	0.007	0.024	0.032	0.056	0.081	0.076	0.101

Fig. 8 Straight thin-walled parts in two processing conditions. **a** Schematic diagram of theoretical values. **b** Hot overlapping. **c** Cold overlapping
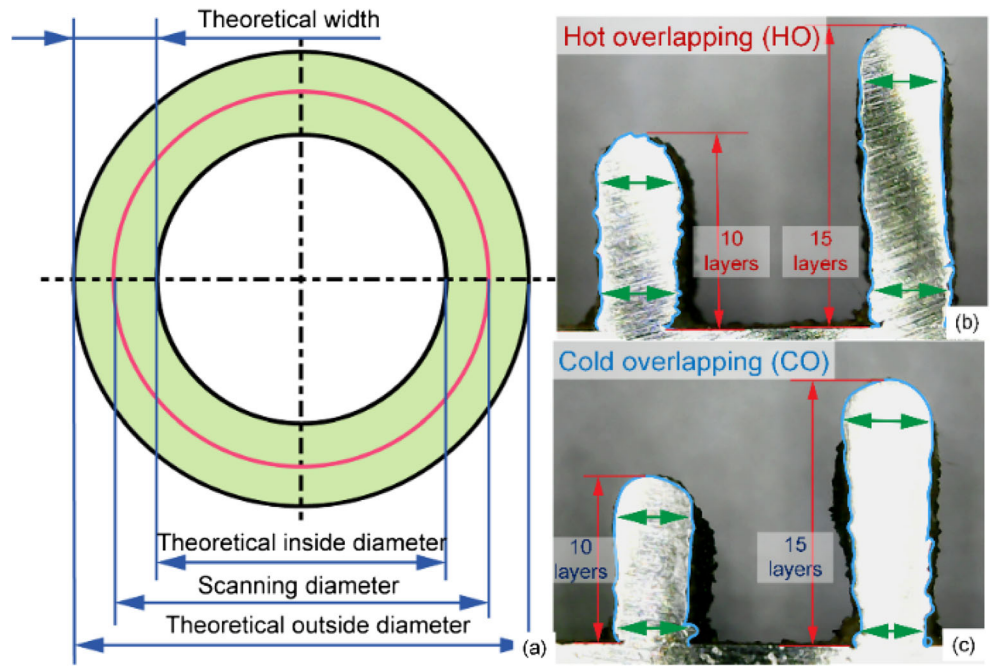
distance between the red line and the upper black line is larger than the lower black line in each small figure, indicating that structural defects such as bending at the top may have more negative effects on cladding later layers.

3. ΔZ_3 and ΔZ_4 (specimen 5, specimen 6, specimen 7) cannot be used as a z-axis increment, because the deviation of the top layers and bottom layers is larger than ΔZ_1 and ΔZ_2 (other four specimens).
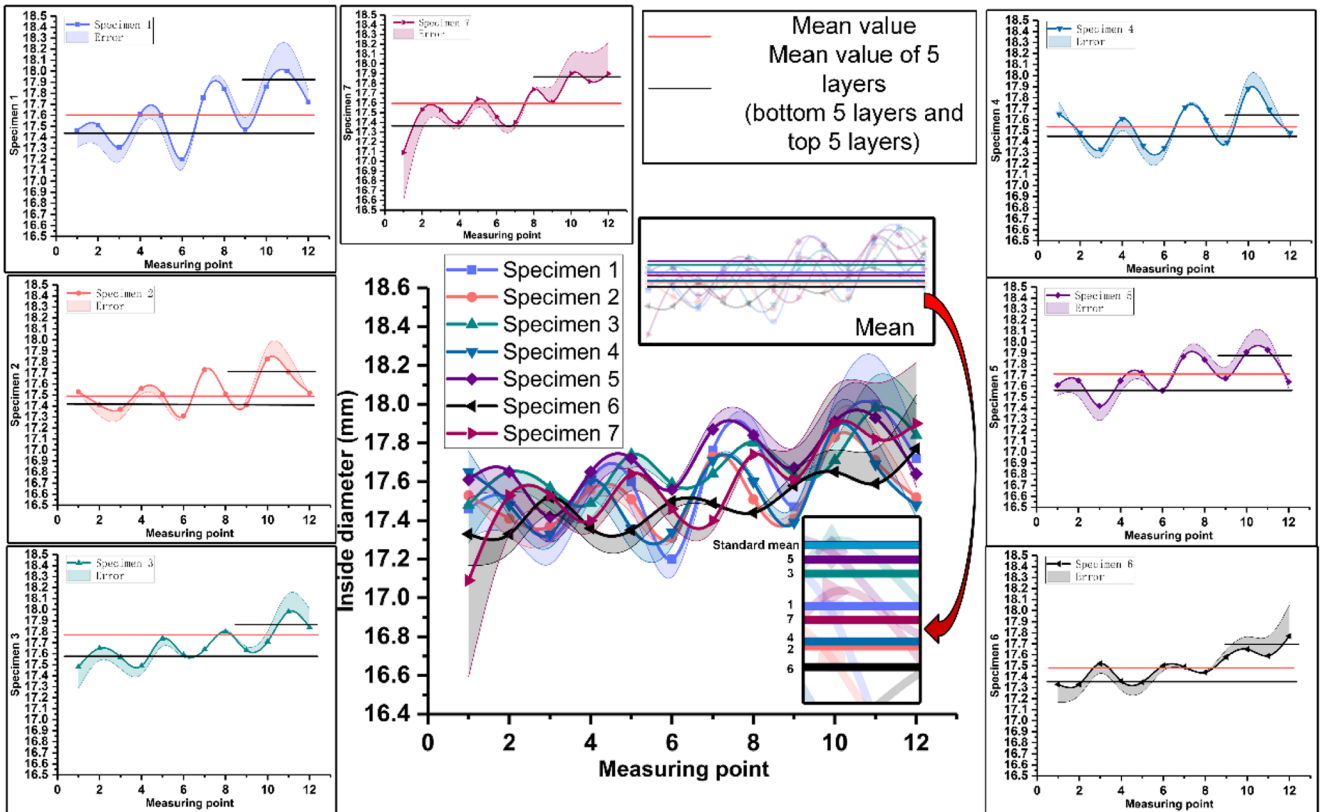
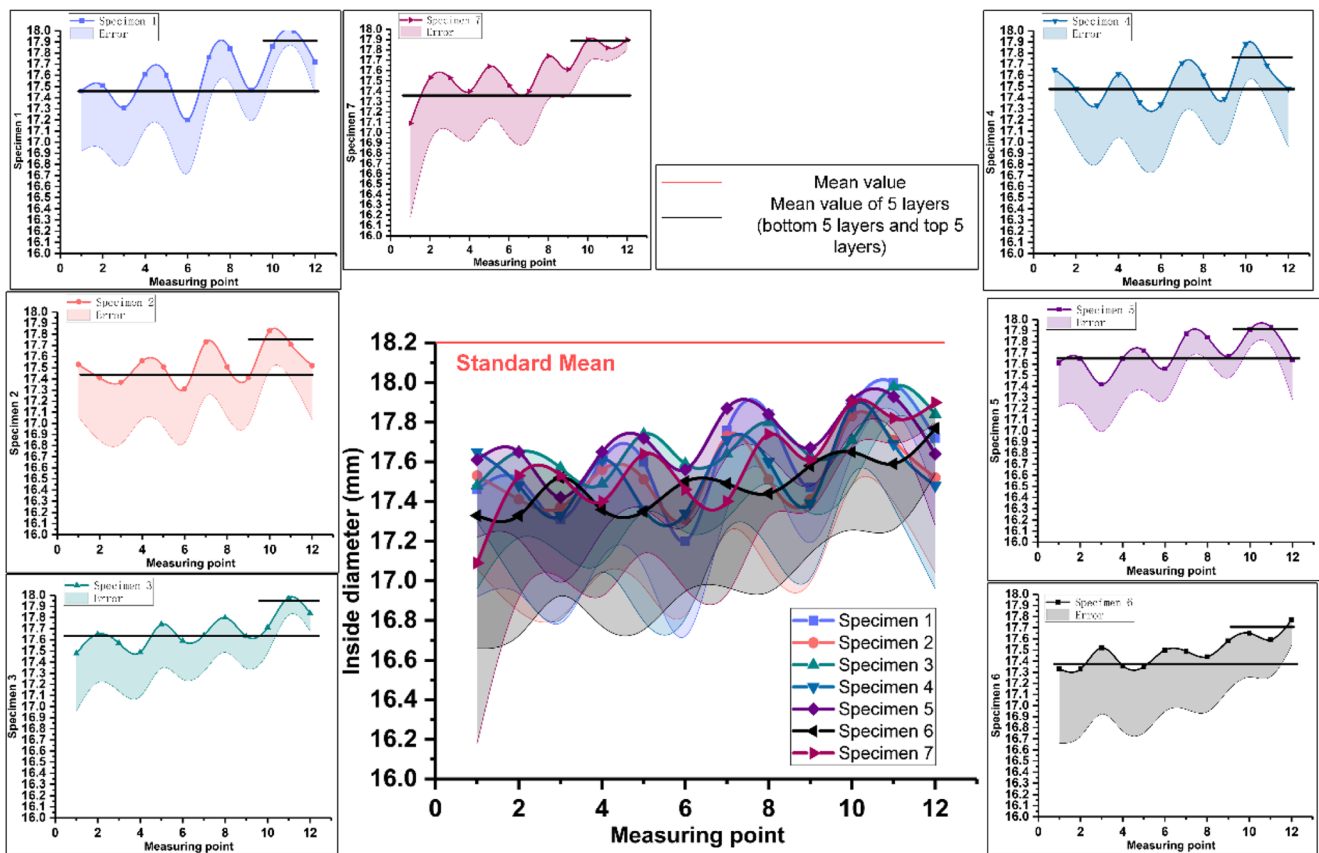**Fig. 9** The deviation between the measured value of the inside diameter and the mean value

Fig. 10 The deviation between the measured value of the inside diameter and the theoretical value
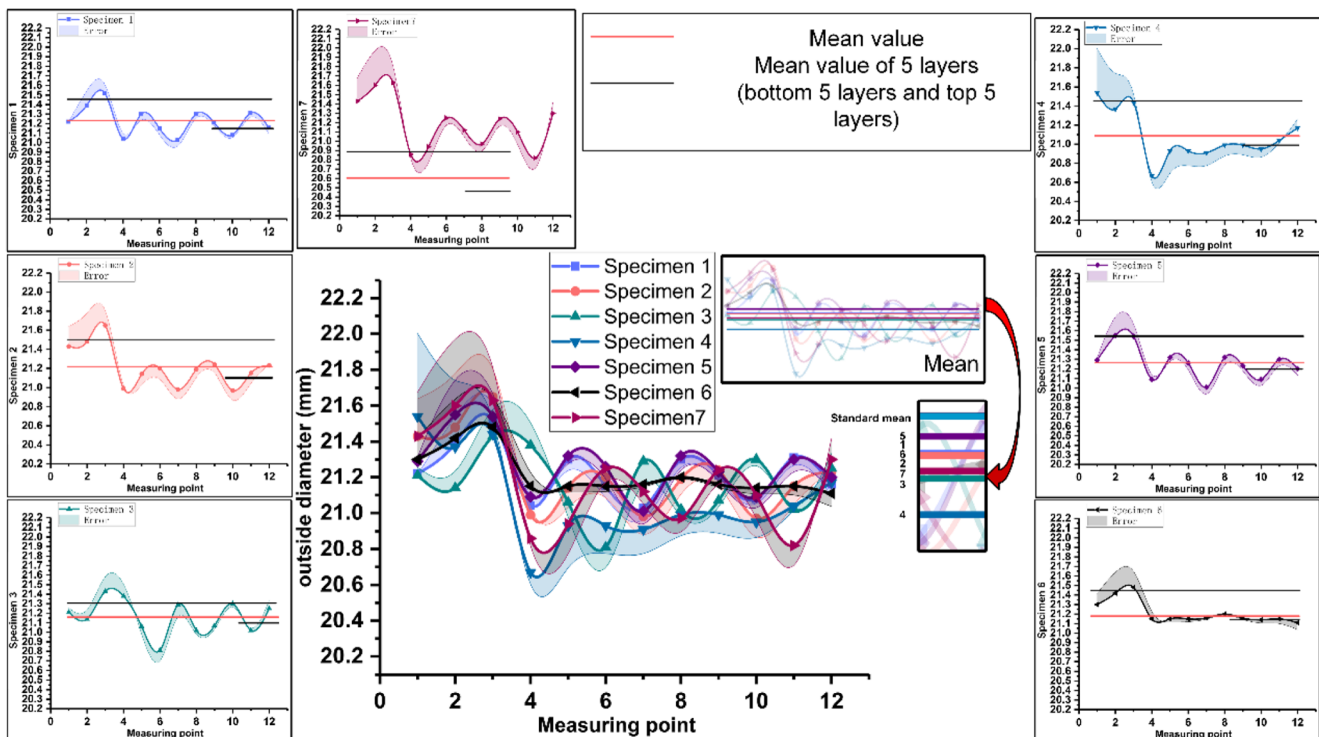

Fig. 11 The deviation between the measured value of the outside diameter and the mean value
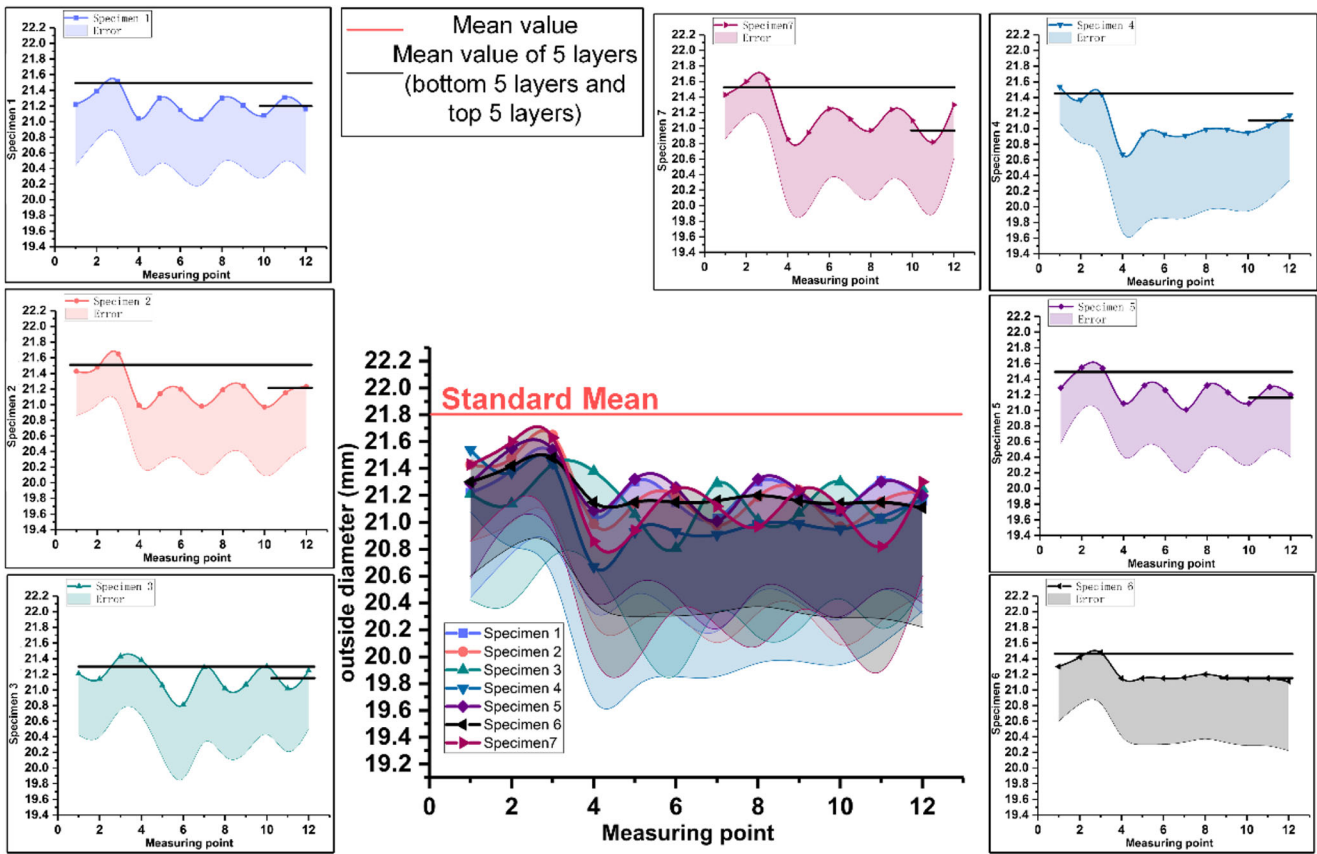
Fig. 12 The deviation between the measured value of the outside diameter and the theoretical value
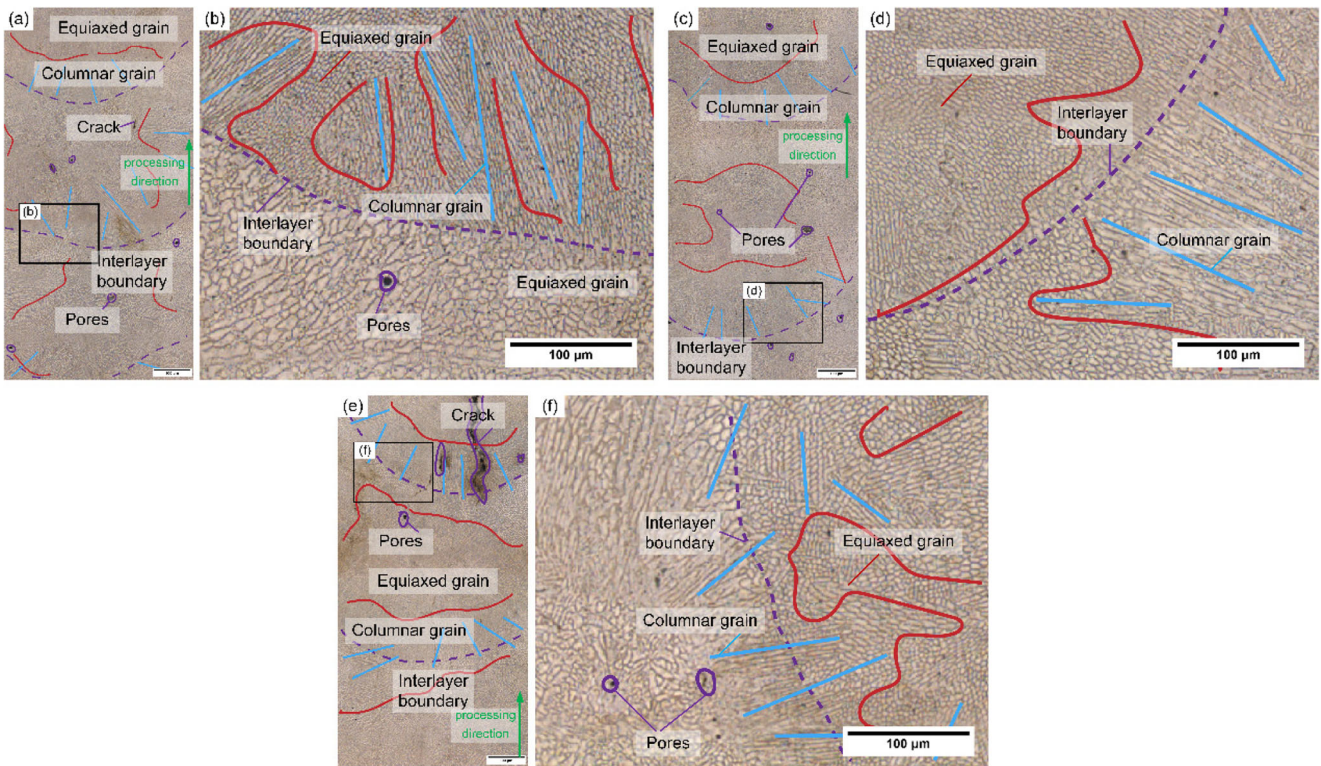

Fig. 13 Microstructure of specimens 1, 2, and 3. **a** Microstructure of Specimen 1. **b** Enlargement figure. **c** Microstructure of Specimen 2. **d** Enlargement figure. **e** Microstructure of Specimen 3. **f** Enlargement figure
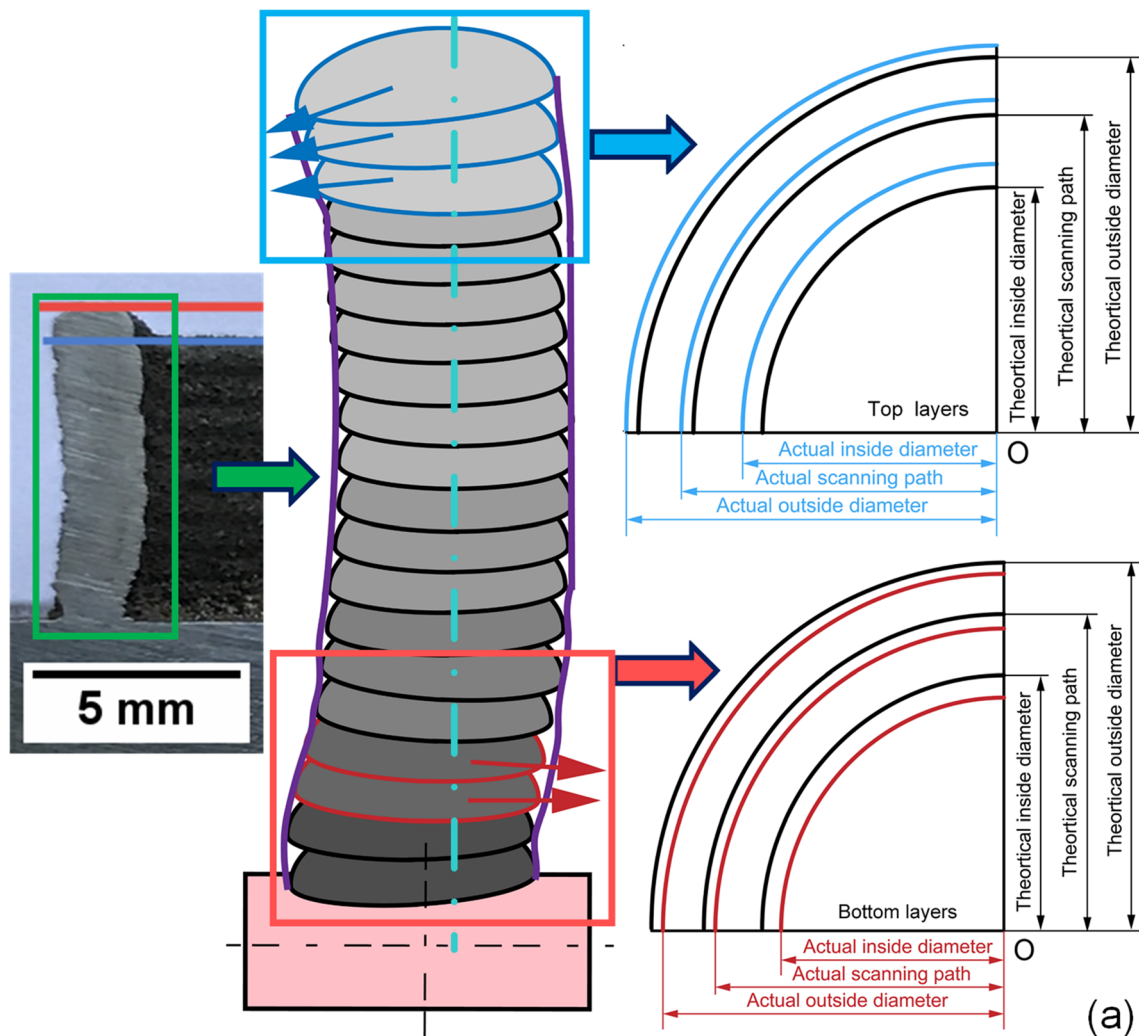
Fig. 14 Schematic figure of morphological defects

3.1.2 Comparison of measured inside diameters with theoretical value

The conclusions are as follows.

1. The bottom deviation of inside diameter is larger, while the middle and upper deviations are smaller (in Fig. 10). It can be seen from the small figures that the deviation bands are more obvious at the bottom. Also, the trend of the deviation bands to the top area shows that the diameter of the thin-walled cylinders increase gradually with increasing height and gradually approach the theoretical value of 18.2 mm. As a result, this phenomenon may cause a relatively large deformation in the bottom region.

2. ΔZ_3 and ΔZ_4 (specimen 5, specimen 6, specimen 7) would not be used as a z-axis increment owing to the larger deviation bands.

3. The thin-walled cylinders have an inward tendency owing to the width that is extended in the direction of the inside

diameter. Because it is shown that the lines of mean values of all specimens are located lower than the standard mean.

3.1.3 Comparison of measured outside diameters with mean values

The conclusions are as follows.

1. In Fig. 11, HO has better forming quality and greater shape accuracy. Specimen 1 and specimen 3 have less deviation bands, which indicates that HO would have better quality and precision. Also, it can be verified according to the order of mean values. The bottom deviation of outside diameter is larger than the middle and upper deviations, which concludes that the thin-walled cylinders have an inward tendency. Also, it means that the outside diameters decrease gradually with increasing height and

Fig. 15 Changes of the working distance owing to the inclination angle
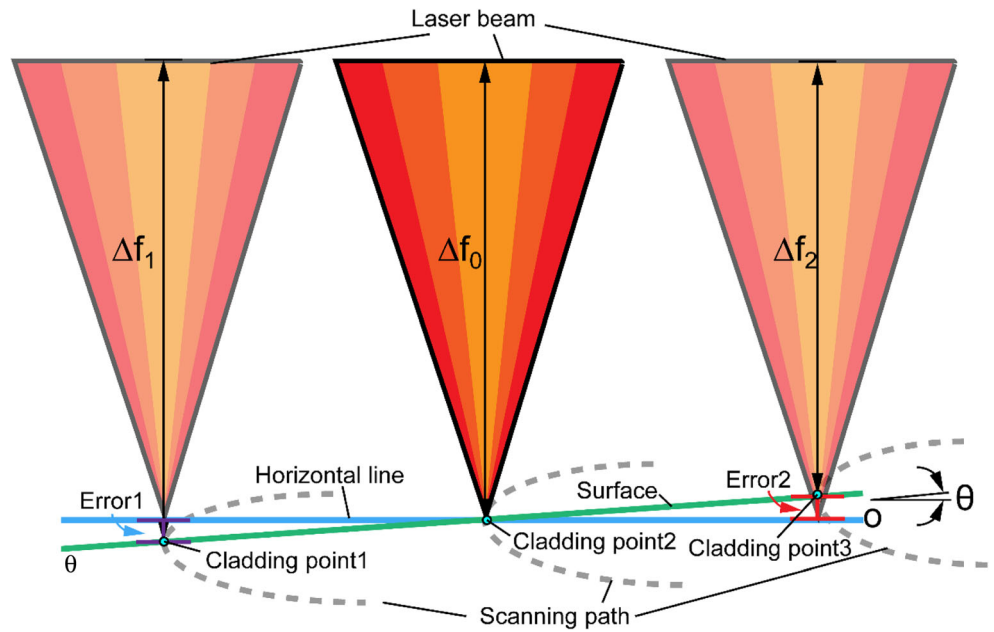
gradually approach the theoretical value of 21.8 mm. Obviously, inevitable improvements in the bottom region of thin-walled cylinder should be conducted.

2. ΔZ_1 and ΔZ_2 are better than ΔZ_3 and ΔZ_4 because of the size of deviation bands. Also, according to the deviation of the top layers and bottom layers, we can draw the same conclusion.
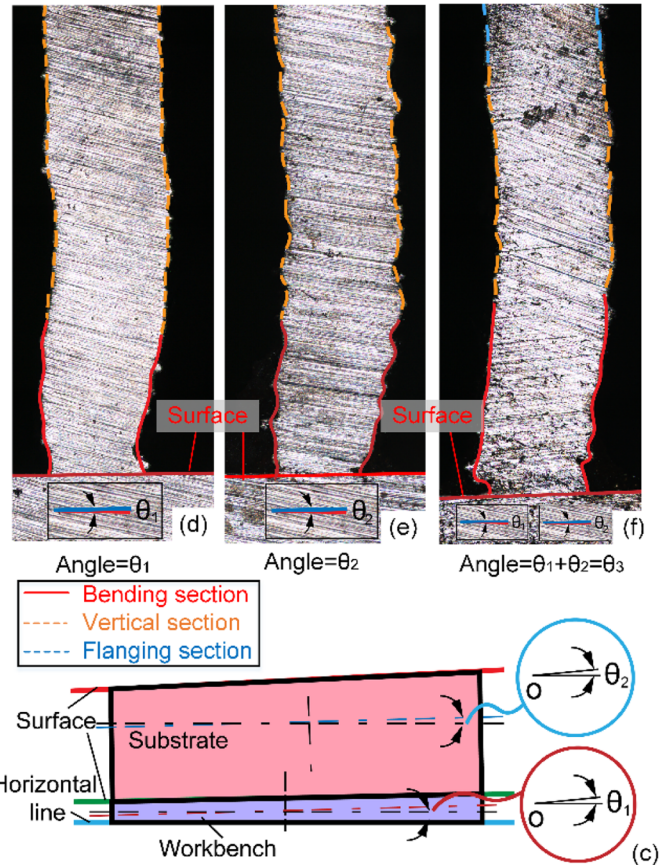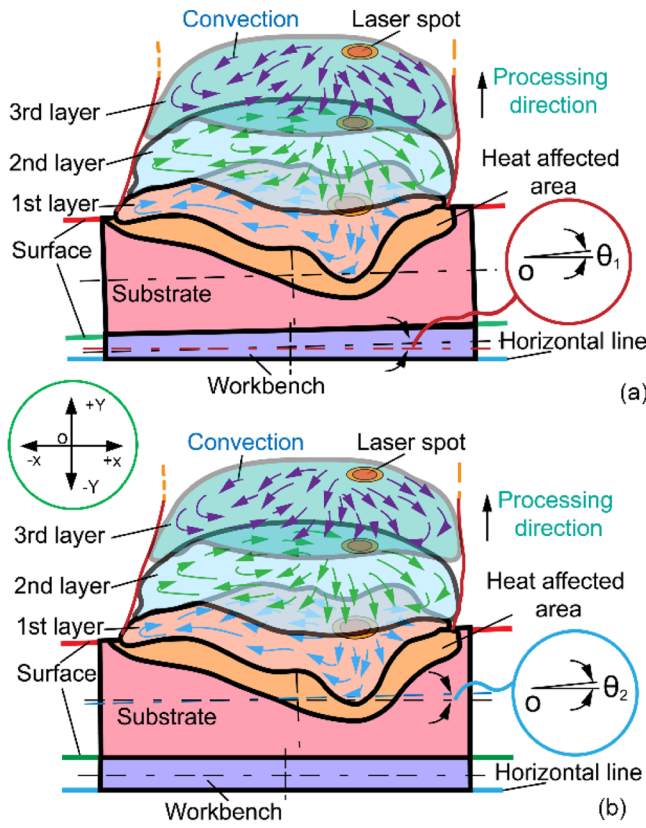

Fig. 16 Schematic figures of different inclination angles and cross sections. **a** Inclination angles θ_1. **b** Inclination angles θ_2. **c** Inclination angles θ_3

3.1.4 Comparison of measured outside diameters with theoretical value

In Fig. 12, the outer diameter decreases with the increase of height. Thin-walled cylinders followed the trend toward inside, so caused larger deviation bands of all specimens. In addition, the deviation of the bottom is small, and the deviation increases as the height increases.

3.2 Microstructure evaluation

Results show that many well-aligned austenitic dendrites vertically orient, forming large columnar grains in the middle region and some dendrites bent toward the surfaces of former layers and forming small columnar grains near the edges [13]. Figure 13b, d, f is a partial enlargement of Fig. 13a, c, e of the microstructures of specimens 1, 2, and 3, respectively. As we can see, the difference of microstructures of the processing direction is not obvious, the organization is uniform, dense, and compact. As a result, we can get refined grains in specimen 2, which uses the CO mechanism because grains are slightly smaller than specimens 1 and 3 (HO mechanism) and evenly distributed, and the forming part has more time to obtain better heat dissipation. Additionally, there exist large visible cracks and pores in specimen 3, which were fabricated via a z-axis increment of 0.266 mm. So, it is of the conviction that ΔZ_1 is the best z-axis increment to obtain more precise morphological feature and finer microstructure.

3.3 Defect analysis and processing optimization

From previous analyses, it can be obtained that the deviation of inside diameter is larger at the bottom, smaller at the top, and the cladding layers are inclined inward at the bottom. On the contrary, the deviation of the outside diameter is smaller at the bottom, larger at the top, and the cladding layers are inclined outward at the top (Fig. 14).

A phenomenon can be observed that the cladding layers are shifted in the direction of the center so that the deviation increases. Moreover, the subsequent layers fabricated on the previous layers are unable to offset the deviation from the theoretical value substantially. After that, the deviation of the outside diameter and theoretical value increased again owing to bending and warping on the top region.

There are several reasons to explain this phenomenon briefly. First, inappropriate ΔZ would cause forming failure. Second, changes in the working distance between the lens and the workbench could result in error during the process. Third, the surface of substrate lacks preheating, which could lead to this feature. All the possible reasons were analyzed, and the improvements and solutions were drawn as follows.

3.3.1 Analyses and improvements of inappropriate delta Z

Previous analyses have drawn a conclusion, which indicates that ΔZ_1 is better than other z-axis increments. So if we select ΔZ_1 as a z-axis increment, it is reasonable to obtain better surface quality and mechanical behaviors comprehensively.

3.3.2 Analyses and improvements of working distance and inclination angle

In the cladding process, the focus lens is installed in the welding nozzle. The working distance between the nozzle and the workbench changes, resulting in the change of the defocus amount (Fig. 15). The cause of the changing working distance is mainly due to uneven surfaces of the workbench, assembly deviations, workbench deformation, and inclination angles between the horizontal line and the workbench surface.

In Fig. 15, the working distance changes owing to the inclination angle between the horizontal line and the workbench surface, which leads to inappropriate defocus amounts Δf_1 and Δf_2 as well as error 1 and error 2 even in the same condition of laser beam and scanning path. From an observation of the inclination condition of cladding parts, substrate, and workbench, we can be informed that in the bottom areas and part of the top regions of the thin-walled structures exist varying degrees of bending and warping defects as shown in Fig. 15.

In Fig. 16, the source of inclination angle is divided into three types. Because the upper surface of the workbench is not horizontal, the upper and lower surfaces of the substrate are not horizontal, which produce an inclination angle θ_1 (Fig. 16a). Also, the upper surface of the workbench is horizontal; the upper and lower surfaces of the substrate are not horizontal leading to an inclination angle θ_2 (Fig. 16b). Finally, the upper surfaces of the workbench and the upper and lower surfaces of the substrate are both not horizontal resulting in an inclination angle θ_3 (Fig. 16c). Besides, Fig. 16d, e, f are cross sections corresponding to three inclination angles, respectively. It can be seen that there exists bending defections at the bottom of fabricated layers, leading to unreliable properties.

There exists an inclination angle in Fig. 16a, the entrance point of the laser beam is marked. When the first layer is cladding, the gravity of the molten pool due to the height difference caused by the inclination angle θ_1 causes the molten pool to move in the − X direction, the center of the molten pool moves in the − X direction at the same time. When the second layer is cladding, the negative influence of the inclination gradually improves due to the redistribution of the tension, convection, and solidification of the upper cladding layer. Also the inclination as well as the height difference gradually decrease, so that the center of the molten pool moves to the + X direction. As time goes by, angles are modified even eliminated by the remelting function of optimized processing condition, forming the vertical fabricated thin wall except the

Table 3 Different inclination angles and height increment

Item	θ (°)	Δh (mm)
θ_1	1.146	2.074
θ_2	0.229	0.423
$\theta_3 = \theta_1 + \theta_2$	1.375	2.505

bending bottom region eventually. Figure 16b, c follows the same principle. Specially, the structure of Fig. 16c needs more time to process vertical structures owing to the inclination angle that is bigger than others. The substrate has a dimension of 100 mm × 100 mm × 12 mm. The height difference Δh caused by the inclination angle is indicated closely related to each other in Table 3. Evidently, the inclination angle can lead to a negative influence on the good qualities of the parts [16].

There is a convection phenomenon in the cladding metal. Under the irradiation of the laser, the surface tension is different due to the inhomogeneity of the temperature distribution in the molten pool. The lower the temperature, the higher the surface tension is. This difference in surface tension causes the liquid to flow from the low tension zone to the high tension zone [17]. The result of the flow results in a high difference in the surface of the liquid, which in turn drives the liquid metal back again, thus forming convection. The surface of the liquid metal decreases with increasing temperature, so the surface tension distribution of the molten pool gradually increases from the center of the molten pool to the edge as shown in Fig. 17c.

Because of the inclination and convection phenomenon, the defocus amount is changing [18]. But the laser incidence mode does not change, which makes the entrance point and the incident angle change with the change of inclination angle and the change of the cladding morphology of each layer. According to Paul et al. [19], a fabricated track is significantly influenced by

gravity, cladding height, and processing parameters (laser powder and powder feed rate) in the moving melting pool model.

According to the Newtonian internal friction law, the moving molten pool model can be built as follows [20, 21]. In Eq. (4), θ_1 means an angle between the z-axis of the molten pool and the gravity G, γ means the surface tension on the outer boundary of the molten pool, μ_L signifies dynamic viscosity, $u_x(z)$ is the flow rate of the z point of the surface of the molten pool, F_{gas} is the force of shielding gas and delivery gas. The flow of molten metal may be described as

$$\mu_L \frac{\partial u_x(z)}{\partial z} = \rho_L gz\sin\theta - \frac{d\gamma}{dT}\frac{\partial T}{\partial s} \quad (4)$$

Where ρ_L is the material density of the liquid metal, T means the temperature of the molten pool, $\partial u_x(z)/\partial z$ is the velocity gradient of the fluid layer in the z direction, s represents the length element of the boundary of the pool surface, $(d\gamma/dT)(\partial T/\partial s)$ is the surface tension component.

$$\frac{d\gamma}{dT} = \gamma_1 = -A_\gamma - R_g\Gamma_s\ln(1 + Ka_i) - \frac{Ka_i}{(1 + Ka_i)}\frac{\Gamma_s\Delta H_0}{T} \quad (5)$$

Where A_γ is the surface tension gradient constant, A_γ is a gas constant, Γ_s means the saturated surface adsorption capacity, a_i signifies the proportion of the ith material in the pool, ΔH_0 is the standard adsorption heat, K is thermal conductivity of the material.

$$\frac{\partial T}{\partial s} = D_{TS} = \frac{h_c(T - T_{amb})}{K} \quad (6)$$

Where k_1 means the relative constants of enthalpy isolation, h_c is the heat transfer coefficient, T_{amb} is the ambient
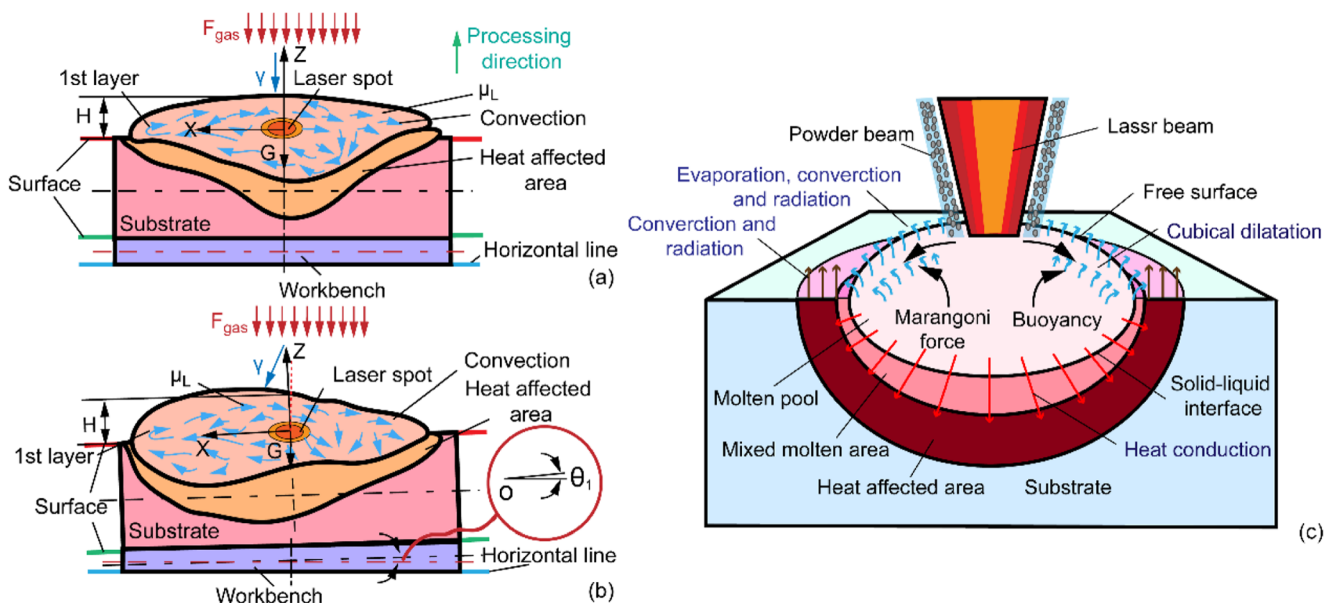

Fig. 17 Moving molten pool model. **a** Molten pool without inclination angles. **b** Molten pool with inclination angle θ_1. **c** Moving molten pool model
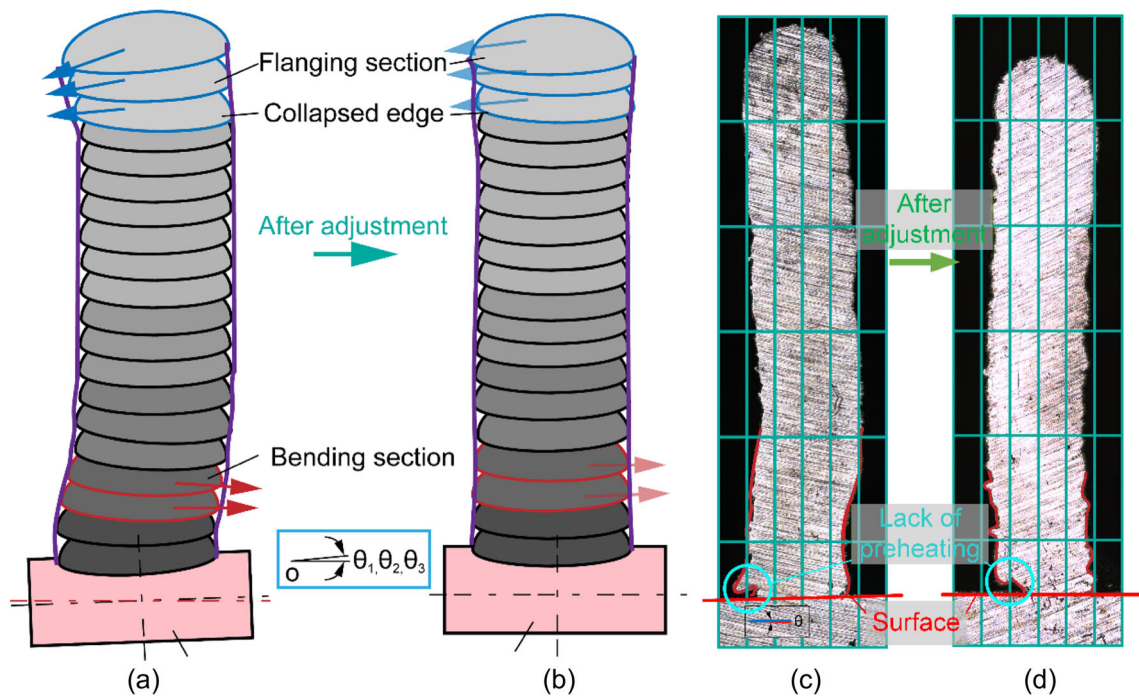
Fig. 18 Schematic figure of adjustment. **a** Non - horizontal substrate or workbench. **b** Horizontal substrate and workbench. **c** Non - horizontal substrate. **d** Horizontal substrate

temperature, substitute Eqs. (5) and (6) into Eq. (4), then integrate z, the flow of molten metal is then derived, which is

$$\mu_L u_x(z) = \rho_L g \frac{z^2}{2} \sin\theta - \gamma_1 D_{TS} z \qquad (7)$$

Where the boundary condition is $z = 0$ and $u_x(z) = 0$, displacement from $t = 0$ to $t = d/v$ is given as

$$x(z) = u_x(z)t = \frac{d}{v\mu_L}\left(\rho_L g \frac{z^2}{2}\sin\theta - \gamma_1 D_{TS} z\right) \qquad (8)$$

Where d is the invariable diameter of the laser spot. In order to eliminate this shortcoming, ensure the horizontal surfaces, two effective strategies can be adopted to improve and adjust accordingly.

First, eliminating or alleviating the inclination angle from Table 2. Second, decreasing the powder flow rate, increasing scanning speed, which can avoid molten pool excessive moving effectively, alleviate defects, and improve forming quality according to Eq. (8).

Figures of the adjustment can be seen in Fig.18a, b. Meanwhile, a grid diagram of cladding thin-walled cylinder

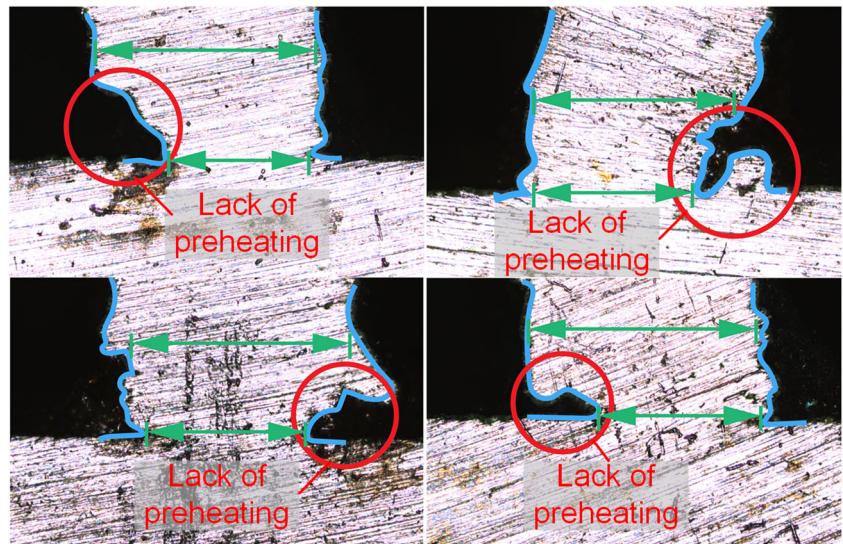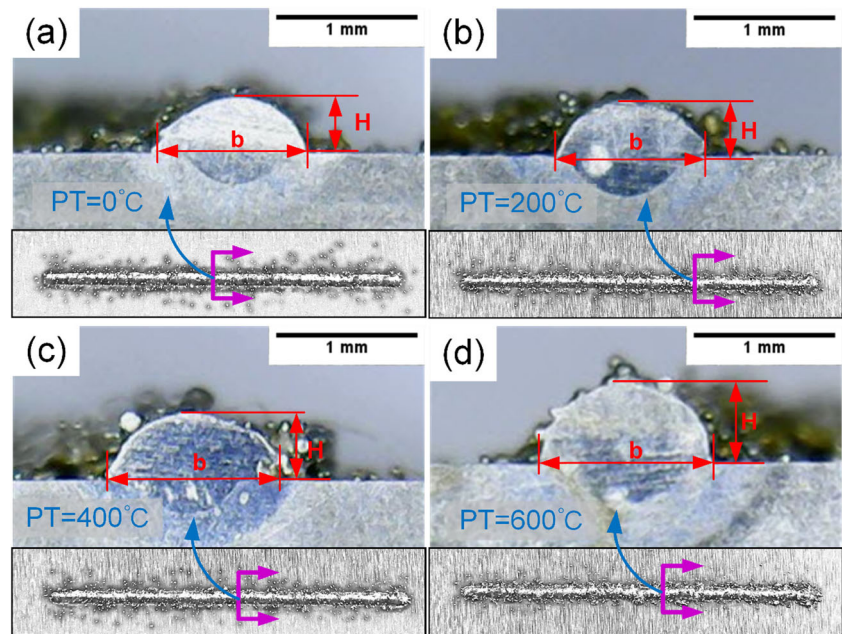**Fig. 19** The deformation of non-preheated parts

Fig. 20 Cross-sectional figures at different preheating temperatures. **a** PT = 0 °C. **b** PT = 200 °C. **c** PT = 400 °C. **d** PT = 600 °C

can assist to measure the effects of adjustment. The morphological features are better than defective structures in Fig. 18c, and the straight wall is almost a vertical line with less bending sections in Fig. 18d. However, there exists a forming defect in the surface of the substrate due to lack of preheating, which will be analyzed later.

3.3.3 Analyses and improvements of lack of preheating

Substrate preheating can effectively reduce the residual stress of the parts, preventing cracking deformation and improving the quality of fabricated parts [13]. The heat dissipation condition in the molten pool of the current layer closely depends on the deposition direction of fore layer [13]. The absorption coefficient of metal material (A_t) increases with the substrate preheating temperature (t) increases, Eq. (4) is explored as follows.

$$A_t = A_{20°C}[1 + \beta(t-20)] \tag{9}$$

Table 4 Different preheating temperature, height, and width of cladding layers

Item	PT (°C)	H (mm)	b (mm)
1	Without preheating	0.320	1.113
2	200	0.444	1.234
3	300	0.466	1.443
4	400	0.591	1.570
5	500	0.608	1.793
6	600	0.610	1.820

Where β is a constant, generally $A_{1000°C} \leq 5A_{20°C}$, most metal absorption coefficients are $1 \times 10^5 - 1 \times 10^6 cm^{-1}$. So, preheating strengthens the ability of the substrate to absorb the laser, the width and the height of the bottom cladding layer increase, which is beneficial to improve the deposition efficiency.

Also, preheating can reduce the temperature gradient of the workbench and the substrate. It was discovered that substrate preheating can result in the least warping for DLF [14]. Additionally, preheating can make the temperature field more uniform and stable and improve the uniformity of the cladding structures [22]. As shown in Fig. 19, the existence of the deformations and defects of parts owes to the lack of the preheated process.

The forming defects are marked with a red circle in Fig. 19. It can be observed that the wall thicknesses of the middle parts are almost the same, because the latter layer is preheated by the former layer (as the new substrate). However, the wall thickness cannot be guaranteed of the theoretical width due to lack of preheating on the substrate [23]. This also can explain the reason why the diameter deviations of the bottom layers are bigger. The following experiments were carried out to verify the conclusion.

The height and width of single cladding layer (Fig. 20) can be obtained, respectively, with other processing parameters unchanged and different preheating temperature (PT). The data can be analyzed from Table 4 that the width and height have increased after preheated.

From Fig. 20, preheating can obviously improve geometrical defects when PT = 400 °C (Fig. 21b). In the HO method, too small preheating temperature cannot get a satisfactory thickness of the thin wall. However, too large preheating temperature will lead to wider wall thickness, microfused powder, and sticky

Fig. 21 Comparison of the cross section about PT in the HO method. **a** Lack of preheating. **b** PT = 400°C. **c** PT = 600°C
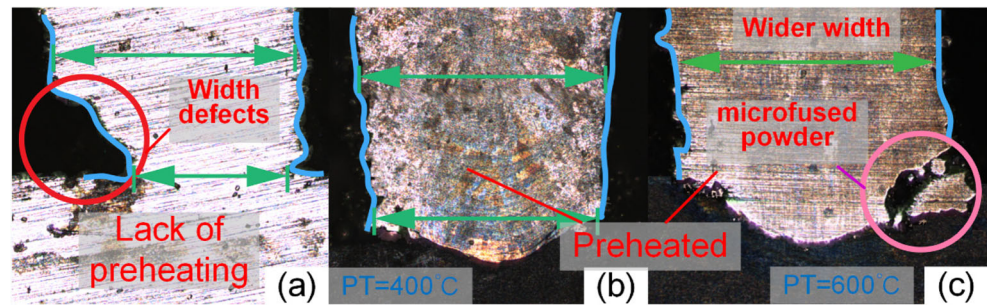
powder phenomenon. (Fig. 21c). Because the molten pool gathers more energy, allowing more powder to enter the molten pool, eventually affecting the shape precision of the parts.

4 Conclusion

To obtain more uniform shape, lesser pores, cracks and sticky powder, flatter outline, and finer microstructures of the LENS-fabricated hollow thin-walled cylinder, the optimal parameter *z*-axis increment of fabricating AISI 316L stainless steel was promoted. Also, the defects of width deviations as well as warping and bending phenomenon of bottom region were explored. Meanwhile, several solutions were drawn to handle these defects respectively and comprehensively. The results of this research are summarized as follows when fabricating hollow thin-walled cylinders.

1. It is proved that a *z*-axis increase of 0.224 mm can obtain better geometrical features and metallurgical behaviors with other processing parameters (laser power, shielding gas flow rate, scanning speed, and powder feed rate) confirmed.
2. Hollow cylinder fabricated via hot overlapping (HO) has better forming quality and shape accuracy, whereas cold overlapping (CO) has finer mechanical behaviors and metallurgical properties.
3. It can be obtained that the deviation of inside diameter is larger at the bottom, smaller at the top, and the cladding layers are inclined inward at the bottom. On the contrary, the deviation of outside diameter is smaller at the bottom, larger at the top, and the cladding layers are inclined outward at the top.
4. Inappropriate *z*-axis increment, changes in the working distance between the lens and the workbench, such as the uneven surface of the substrate and various inclination angles (angle theta 1, theta 2, and theta 3), thermal beam focusing, and lack of preheating can cause deformation and defects. Additionally, these defects can be modified, then obtain a satisfied thin-walled parts. For instance, alleviation of the deviation of working distance, improvement and modification of the inclination angles, and

appropriate preheating temperature (PT = 600 °C) are both practical strategies to obviate defects.

References

1. Zhang K, Wang S, Liu W, Shang X (2014) Characterization of stainless steel parts by laser metal deposition shaping. Mater Des 55:104–119. https://doi.org/10.1016/j.matdes.2013.09.006
2. Karczewski K, Dąbrowska M, Ziętala M, Polański M (2017) Fe-Al thin walls manufactured by laser engineered net shaping. J Alloys Compd 696:1105–1112. https://doi.org/10.1016/j.jallcom.2016.12.034
3. Wang X, Deng D, Qi M, Zhang H (2016) Influences of deposition strategies and oblique angle on properties of AISI316L stainless steel oblique thin-walled part by direct laser fabrication. Opt Laser Technol 80:138–144. https://doi.org/10.1016/j.optlastec.2016.01.002
4. Wang X, Deng D, Yi H, Xu H, Yang S, Zhang H (2017) Influences of pulse laser parameters on properties of AISI316L stainless steel thin-walled part by laser material deposition. Opt Laser Technol 92: 5–14. https://doi.org/10.1016/j.optlastec.2016.12.021
5. Peng L, Shengqin J, Xiaoyan Z, Qianwu H, Weihao X (2007) Direct laser fabrication of thin-walled metal parts under open-loop control. Int J Mach Tools Manuf 47(6):996–1002. https://doi.org/10.1016/j.ijmachtools.2006.06.017
6. Petrat T, Graf B, Gumenyuk A, Rethmeier M (2016) Laser metal deposition as repair technology for a gas turbine burner made of Inconel 718. Phys Procedia 83:761–768. https://doi.org/10.1016/j.phpro.2016.08.078
7. Qi H, Azer M, Singh P (2009) Adaptive toolpath deposition method for laser net shape manufacturing and repair of turbine compressor airfoils. Int J Adv Manuf Technol 48(1–4):121–131. https://doi.org/10.1007/s00170-009-2265-7
8. Abioye TE, Farayibi PK, Kinnel P, Clare AT (2015) Functionally graded Ni-Ti microstructures synthesised in process by direct laser metal deposition. Int J Adv Manuf Technol 79(5–8):843–850. https://doi.org/10.1007/s00170-015-6878-8
9. Niu F, Wu D, Ma G, Wang J, Zhuang J, Jin Z (2016) Rapid fabrication of eutectic ceramic structures by laser engineered net shaping. Procedia CIRP 42:91–95. https://doi.org/10.1016/j.procir.2016.02.196
10. Durejko T, Ziętala M, Polkowski W, Czujko T (2014) Thin wall tubes with Fe3Al/SS316L graded structure obtained by using laser

engineered net shaping technology. Mater Des 63:766–774. https://doi.org/10.1016/j.matdes.2014.07.011

11. de Lima MSF, Sankaré S (2014) Microstructure and mechanical behavior of laser additive manufactured AISI 316 stainless steel stringers. Mater Des 55:526–532. https://doi.org/10.1016/j.matdes.2013.10.016

12. Calleja A, Tabernero I, Fernández A, Celaya A, Lamikiz A, López de Lacalle LN (2014) Improvement of strategies and parameters for multi-axis laser cladding operations. Opt Lasers Eng 56:113–120. https://doi.org/10.1016/j.optlaseng.2013.12.017

13. Jang J-H, Joo B-D, Van Tyne CJ, Moon Y-H (2013) Characterization of deposited layer fabricated by direct laser melting process. Met Mater Int 19(3):497–506. https://doi.org/10.1007/s12540-013-3018-6

14. Klingbeil NW, Beuth JL, Chin RK, Amon CH (2002) Residual stress-induced warping in direct metal solid freeform fabrication. Int J Mech Sci 44(2002):57–77

15. PengL. (2004) Direct laser fabrication of 3-dimensional metal parts based on laser cladding. (in Chinese) Dissertation of Huazhong University of Science & Technology: 114

16. Arrizubieta JI, Lamikiz A, Klocke F, Martínez S, Arntz K, Ukar E (2017) Evaluation of the relevance of melt pool dynamics in Laser Material Deposition process modeling. Int J Heat Mass Transf 115:80–91. https://doi.org/10.1016/j.ijheatmasstransfer.2017.07.011

17. Yin H, Felicelli SD (2010) Dendrite growth simulation during solidification in the LENS process. Acta Mater 58(4):1455–1465. https://doi.org/10.1016/j.actamat.2009.10.053

18. Wang L, Felicelli S, Gooroochurn Y, Wang PT, Horstemeyer MF (2008) Optimization of the LENS® process for steady molten pool size. Mater Sci Eng A 474(1–2):148–156. https://doi.org/10.1016/j.msea.2007.04.119

19. Paul CP, Mishra SK, Kumar A, Kukreja LM (2013) Laser rapid manufacturing on vertical surfaces: analytical and experimental studies. Surf Coat Technol 224:18–28. https://doi.org/10.1016/j.surfcoat.2013.02.044

20. Dai D, Gu D, Zhang H, Xiong J, Ma C, Hong C, Poprawe R (2018) Influence of scan strategy and molten pool configuration on microstructures and tensile properties of selective laser melting additive manufactured aluminum based parts. Opt Laser Technol 99:91–100. https://doi.org/10.1016/j.optlastec.2017.08.015

21. Gan Z, Liu H, Li S, He X, Yu G (2017) Modeling of thermal behavior and mass transport in multi-layer laser additive manufacturing of Ni-based alloy on cast iron. Int J Heat Mass Transf 111:709–722. https://doi.org/10.1016/j.ijheatmasstransfer.2017.04.055

22. Vasinonta A, Beuth JL, Griffith ML (2001) A process map for consistent build conditions in the solid freeform fabrication of thin-walled structures. J Manuf Sci Eng 123(4):615. https://doi.org/10.1115/1.1370497

23. Kim H, Liu Z, Cong W, Zhang HC (2017) Tensile fracture behavior and failure mechanism of additively-manufactured AISI 4140 low alloy steel by laser engineered net shaping. Materials (Basel) 10(11). https://doi.org/10.3390/ma10111283